

PAPER

## Direct nanomechanical measurements of boron nitride nanotube—ceramic interfaces

To cite this article: Chenglin Yi *et al* 2019 *Nanotechnology* **30** 025706

View the [article online](#) for updates and enhancements.



**IOP | ebooks™**

Bringing you innovative digital publishing with leading voices to create your essential collection of books in STEM research.

Start exploring the collection - download the first chapter of every title for free.

# Direct nanomechanical measurements of boron nitride nanotube—ceramic interfaces

Chenglin Yi<sup>1</sup>, Soumendu Bagchi<sup>2</sup>, Feilin Gou<sup>1</sup>,  
Christopher M Dmuchowski<sup>1,3</sup>, Cheol Park<sup>4</sup>, Catharine C Fay<sup>4</sup>,  
Huck Beng Chew<sup>2,5</sup> and Changhong Ke<sup>1,3,5</sup> 

<sup>1</sup> Department of Mechanical Engineering, State University of New York at Binghamton, Binghamton, NY 13902, United States of America

<sup>2</sup> Department of Aerospace Engineering, University of Illinois at Urbana-Champaign, Urbana, IL 61801, United States of America

<sup>3</sup> Materials Science and Engineering Program, State University of New York at Binghamton, Binghamton, NY 13902, United States of America

<sup>4</sup> Advanced Materials and Processing Branch, NASA Langley Research Center, Hampton, VA 23681, United States of America

E-mail: [cke@binghamton.edu](mailto:cke@binghamton.edu) and [hbchew@illinois.edu](mailto:hbchew@illinois.edu)

Received 18 June 2018, revised 31 August 2018

Accepted for publication 15 October 2018

Published 2 November 2018



## Abstract

Boron nitride nanotubes (BNNTs) are a unique class of light and strong tubular nanostructure and are highly promising as reinforcing additives in ceramic materials. However, the mechanical strength of BNNT-ceramic interfaces remains largely unexplored. Here we report the first direct measurement of the interfacial strength by pulling out individual BNNTs from silica (silicon dioxide) matrices using *in situ* electron microscopy techniques. Our nanomechanical measurements show that the average interfacial shear stress reaches about 34.7 MPa, while density functional theory calculations reveal strong bonded interactions between BN and silica lattices with a binding energy of  $-6.98 \text{ eV nm}^{-2}$ . Despite this strong BNNT-silica binding, nanotube pull-out remains the dominant failure mode without noticeable silica matrix residues on the pulled-out tube surface. The fracture toughness of BNNT-silica ceramic matrix nanocomposite is evaluated based on the measured interfacial strength property, and substantial fracture toughness enhancements are demonstrated at small filler concentrations.

Keywords: nanotube-ceramic interface, boron nitride nanotubes, ceramic matrix nanocomposites, fracture toughness, pull-out experiments

(Some figures may appear in colour only in the online journal)

## 1. Introduction

The envisioned lightweight and high strength and toughness characteristics of fiber-reinforced ceramic matrix nanocomposites (CMNC) are highly attractive for the aerospace, automotive and chemical industries [1]. With the addition of a low concentration of reinforcing filler materials, CMNC not only inherit the excellent physical properties of the underlying matrix material (e.g. superior hardness, chemical inertness and retention of strength at high temperatures [2]), but also

overcome or mitigate their intrinsic weakness of brittleness that greatly limits their usage and add new functionalities that are attributed to the fiber's physical characteristics. Selection of appropriate reinforcing filler materials is key to the bulk property enhancement in fiber-reinforced CMNC. Boron nitride nanotubes (BNNTs) [3, 4] are a type of light and strong tubular nanostructure with many extraordinary material properties and are promising as filler materials for CMNC. Research reveals that BNNTs are an axially strong and transversely supple material, as compared to their pure carbon counterpart, carbon nanotubes (CNTs). BNNTs reportedly possess a Young's modulus of up to 1.3 TPa and a tensile

<sup>5</sup> Authors to whom any correspondence should be addressed.

strength of up to 33 GPa [5–14], both of which are comparable to those reported for CNTs. However, the reported transverse modulus of BNNTs is substantially lower than that of comparable CNTs [15–17]. It is therefore energetically more favorable for BNNTs, than comparable CNTs, to bend and conform to ceramic grain surfaces, which is critical to the improvement of fracture toughness or other physical properties that rely on an intimate tube-matrix interface (e.g. thermal conductivity). BNNTs also possess piezoelectric and radiation shielding characteristics [18, 19], extraordinary thermal conductivity [20] and thermal and chemical stabilities [21, 22]. Recent studies reveal that BNNTs possess superior oxidation resistance and are capable of maintaining their structural and mechanical properties at up to 850 °C in air, while CNTs begin to oxidize at temperatures of around 400 °C in air [23]. BNNTs are capable of enduring much higher temperatures in vacuum [24] and are superior in high temperature environments, such as those typically encountered in the processing and/or working conditions of ceramic nanocomposites. Unlike the metallic or semi-conductive properties of CNTs, BNNTs possess a large bandgap of 5–6 eV and thus are excellent insulators [3, 25]. The addition of BNNTs in ceramic matrices enhances their thermal conductivity, while preserving their insulating properties. These extraordinary multifunctional characteristics of BNNT-reinforced CMNC enable their widespread industrial usage, in particular for applications that involve harsh thermal, chemical, and/or radiation environments.

Substantial mechanical property enhancements in BNNT-reinforced CMNC have been reported in the literature. The presence of 4 wt% BNNT in hydroxyapatite composites can increase the strength by 90% and the toughness by 35% [26]. Similarly, the presence of 1 wt% BNNT in zirconia and Al<sub>2</sub>O<sub>3</sub> was reported to increase the toughness by 65% and 35%, respectively [27, 28]. More recently, Du *et al* reported that adding 5 wt% of BNNT in silica (SiO<sub>2</sub>) dramatically increases the fracture strength and toughness by 131% and 109%, respectively, in part due to microstructural changes [29]. To date, a variety of spectroscopy and electron microscopy techniques have been used to elucidate the morphology of BNNTs inside CMNC, microstructural changes of the ceramic matrix, possible reaction products formed on the nanotube-ceramic interface, as well as tube morphology in the fractured composites [27–31]. However, such microscopic observations and bulk mechanical properties measurements can only provide indirect and/or qualitative assessment of the interfacial properties. Quantitative evaluations of the BNNT-ceramic interfacial load transfer characteristics and interfacial binding interactions remain elusive, and will have to be ascertained from microscopic experiments and first principle computations.

In this paper, we quantitatively investigate the interfacial strength between BNNTs and silica using *in situ* electron microscopy single-nanotube pull-out techniques in conjunction with micromechanics modeling and density functional theory (DFT) calculations. The nanomechanical experiments demonstrate that nanotube pull-out resulting from interfacial failure is the major toughening mechanism. The DFT studies report strong interfacial binding interactions between BN and silica,

which explains the high interfacial shear strength measured from the experiments. The potential fracture toughness enhancement in BNNT-silica nanocomposites is predicted based on the measured interfacial strength property and substantial fracture toughness improvements are demonstrated at small filler concentrations. To the best of our knowledge, this nanomechanical study is the *first* quantitative report on the BNNT-ceramic interfacial strength. The findings are useful to better understand the nanotube's reinforcing mechanism in nanotube-reinforced CMNC. This study demonstrates that BNNTs are excellent reinforcing filler materials for light, strong and durable CMNC. The employed nanomechanical experimental technique together with the micromechanics and atomistic theoretical frameworks is readily extendable to the nanomechanical characterization of interfaces in other nanotube/nanofiber-ceramic systems.

## 2. Results and discussion

### 2.1. *In situ* electron microscopy nanomechanical single-tube pull-out measurements

The mechanical strength of BNNT-silica interfaces is characterized by using *in situ* scanning electron microscopy (SEM) nanomechanical single-nanotube pull-out technique, as illustrated in figure 1(a). This testing technique has been successfully used to elucidate the interfacial properties of nanotube-polymer and nanotube-metal composites [32–36]. In this testing scheme, a protruding BNNT from a sandwiched ceramic-tube-ceramic thin-film nanocomposite is incrementally stretched by an atomic force microscopy (AFM) cantilever until the embedded tube segment is completely pulled out of the ceramic matrix. To avoid bending effects, pull-out measurements are only conducted for protruding tubes that are parallel to the axial (stretching) direction of the AFM tip.

The BNNTs employed in this study were synthesized using high-temperature pressure (HTP) methods [37, 38]. HTP-BNNTs reportedly possess highly crystalline structures with a small number of tube walls and possess lengths of up to at least a few hundred microns. Figure 1(b) shows an SEM image of an as-received HTP-BNNT sample, displaying tubes with lengths of over 10 microns. Recent AFM studies reveal that over 97% of the HTP-BNNTs are single- to quadruple-walled [19]. Double-walled structures, as exemplified by the transmission electron microscopy (TEM) image shown in figure 1(c), have a dominant presence (about 57%) and their outer diameters are found to be 1.9–3.9 nm. Such thin shell (i.e. small numbers of tube walls/diameter) structures allow for significant contact of the outermost wall with the surrounding matrix, while the long tubular length allows for substantial load transfer via the tube-matrix interface. However, most of our nanomechanical single-tube measurements are performed using relatively shorter tubes of less than 2 μm in length since the higher bending rigidity allows these tubes to remain straight inside the matrix. Ultrasonication was employed to disperse/separate the tubes and to shorten their

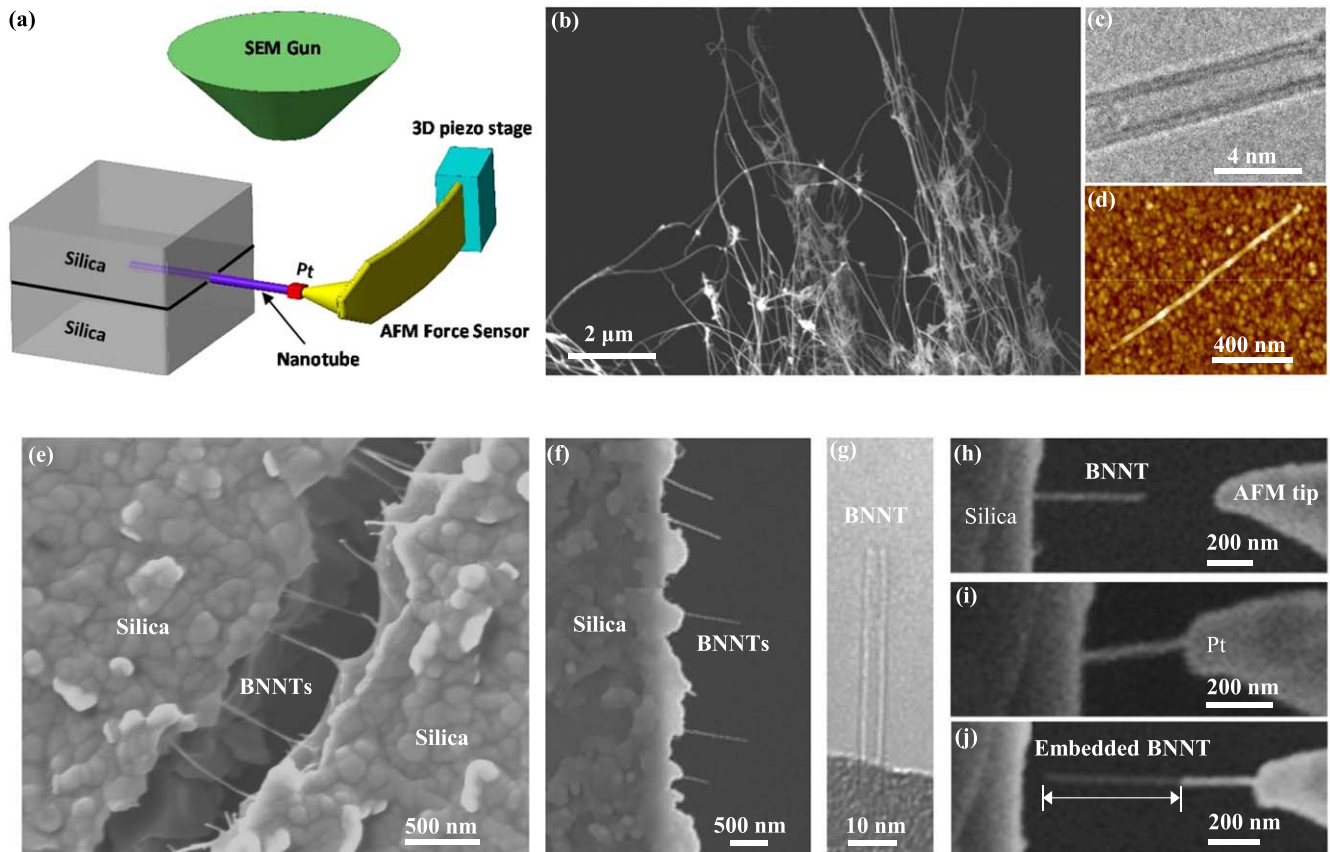


**Figure 1.** *In situ* SEM nanomechanical single-tube pull-out testing scheme (a) and sample preparation and characterization (b)–(f): (b) SEM image of an as-received HTP-BNNT sample. (c) TEM image of a double-walled BNNT of about 3.2 nm in outer diameter. (d) AFM image of one deposited BNNT on an electron beam evaporated silica surface by using spin-coating. (e) SEM image of one fractured silica/BNNT/silica thin-film composite with bridging, pulled-out and fractured BNNTs. (f) SEM of one fractured silica/BNNT/silica thin-film composite with protruding BNNTs that were employed in the pull-out measurements. (g) TEM image of a protruding BNNT of about 3.2 nm in outer diameter from a silica matrix. (h)–(j) Selected SEM snapshots showing a typical single-nanotube pull-out experiment conducted on a BNNT-silica composite sample.

lengths to the desirable level (less than  $2\ \mu\text{m}$ ) [39]. Figure 1(d) shows a typical straight BNNT of about  $1.2\ \mu\text{m}$  in length and about 2.9 nm in diameter, which was spin-coated on an electron-beam deposited silica film with an average grain size of about 25.8 nm. Figure 1(e) shows the fractured surface of a BNNT-silica thin-film nanocomposite bridged by BNNT fibers. In this partially fractured sample, many of the protruded tubes resemble cantilevered or crack-bridging structures, indicating they were pulled out from the ceramic matrix. Figure 1(f) shows the cantilevered tubes protruding from a halved ceramic matrix. As shown by the TEM image in figure 1(g), the protruded tube structures possess pristine surfaces without noticeable matrix residue, suggesting that the BNNT cleanly separates from the silica matrix during pull-out. This conclusively shows that nanotube pull-out is one major failure and energy dissipation mechanism in BNNT-silica nanocomposites.

Figures 1(h)–(j) show three selected SEM snapshots that were recorded during one representative pull-out measurement. The tip of a calibrated AFM probe was first controlled to approach the free end of a selected protruding tube, as shown in figure 1(h). Electron beam induced deposition of Pt [40] was employed to weld the tube's free end to the AFM tip

to ensure a firm attachment, as shown in figure 1(i). Subsequently, the gripped tube was stretched by means of gradually displacing the AFM cantilever until it was fully pulled out of the ceramic film. It is noted that the pull-out test is essentially a force-controlled measurement. The nanotube pull-out event occurred when the pulling force reached a threshold value, which is denoted as the *pull-out* force, and was observed as a catastrophic failure of the tube-ceramic interface. For the tested sample shown in figure 1(j), the applied pull-out force and the embedded tube length were measured to be 158 nN and 536 nm, respectively.

We have tested a number of BNNT-silica samples, and successful single-nanotube pull-out phenomena similar to the one displayed in figure 1(j) were observed for the majority of our pull-out measurements. However, interface failure scenarios resulting in fracturing of nanotubes and telescopic pull-out were also observed, as displayed in the selected SEM snapshots in figure 2. The observed tube fracture occurred in its free-standing cantilevered portion. For the telescopic pull-out, the outermost shell(s) of the nanotube was broken by the stretching force and subsequently the inner tube shell(s) was pulled out. Both these two scenarios suggest a strongly-bonded tube-matrix interface, which allows for effective load

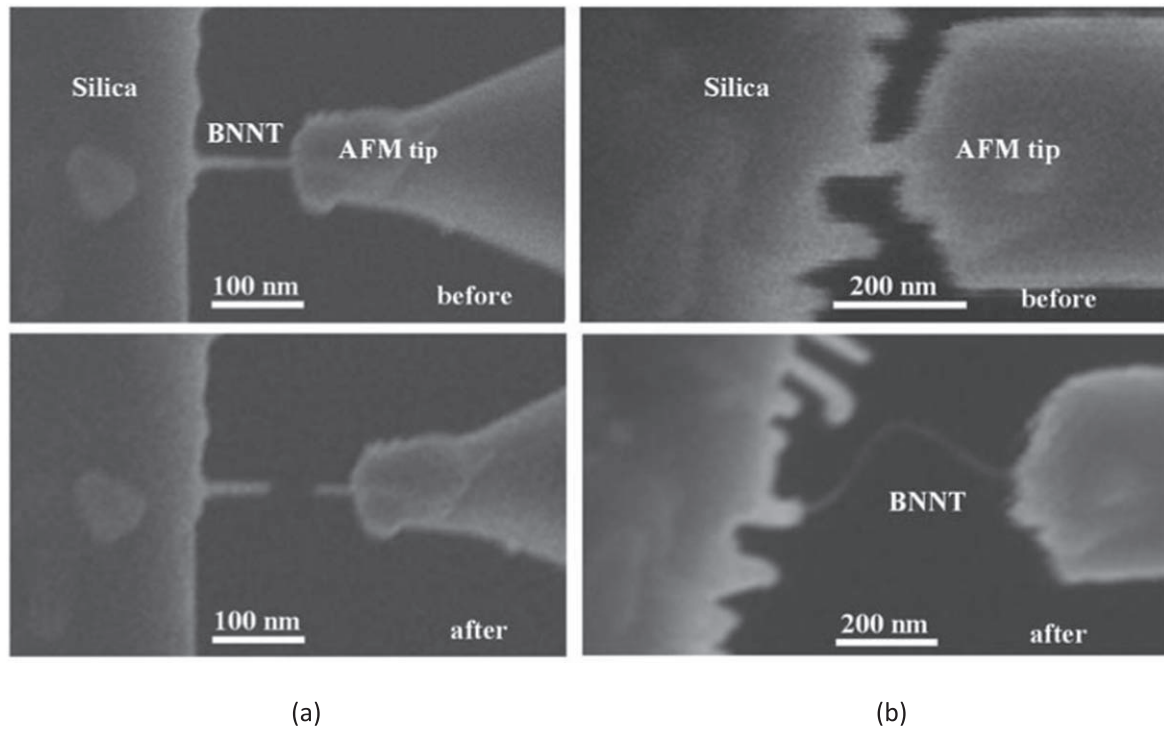


**Figure 2.** Representative SEM snapshots showing (a) fracturing of a nanotube and (b) telescopic pull-out of a nanotube.

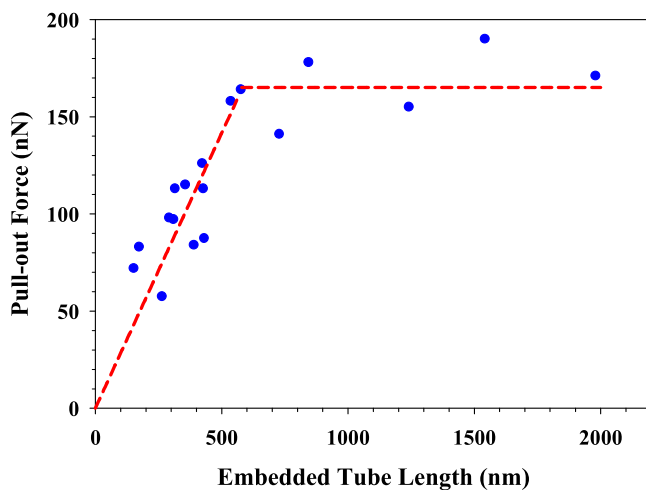


**Figure 3.** The measured pull-out force versus the embedded tube length for BNNT-silica interfaces (solid circle) with the bi-linear fitting curves (dashed lines).

transfer in the BNNT-reinforced silica nanocomposites [41] and contributes to energy dissipation. These two failure scenarios are excluded from our interfacial strength and load transfer analysis of the BNNT-silica interface.

Figure 3 shows the pull-out data from 18 successful single-nanotube pull-out measurements that were conducted on BNNT-silica samples. The pull-out force recorded in these independent measurements is found to range from 57 to 190 nN, while the embedded nanotube length is found to fall between 152 nm and 2.0  $\mu\text{m}$ . It is noticed that the pull-out force initially has a nearly linear dependence with the embedded length, and then remains in a narrow range, forming a plateau. The measured pull-out force versus the embedded

tube length dependence displays a shear lag effect [42]. Similar shear-lag dependences were observed in the nanomechanical studies of nanotube-polymer [32, 33, 35] and nanotube-metal [34, 36] interfaces. Therefore, the shear lag effect is seemingly a universal physical phenomenon governing the interface failure and the energy dissipation in the nanotube-reinforced nanocomposites regardless of the matrix material (polymers, metals or ceramics). The measured pull-out force data set shown in figure 3 is least-square fitted using a bi-linear fitting curve, which is a simplified representation of the shear lag effect and will be used to determine the interfacial load carrying capacity and the interfacial shear stress of the tube-matrix interface. The force plateau represents the load carrying capacity limit of the tested BNNT-silica interface and is found to be  $165 \pm 15$  nN ( $n = 6$ ). The critical embedded length that corresponds to the onset of the force plateau is approximated as the joint value in the bi-linear fitting curve (about 560 nm).

The average interfacial stress strength (IFSS) of BNNT-silica interfaces,  $\tau_{ave}$ , is given as  $\tau_{ave} = \frac{P_{out}}{\pi \times D \times L}$ , in which  $D$  is the nanotube diameter,  $L$  is the embedded tube length and  $P_{out}$  is the pull-out force. Due to the shear lag effect, only those measurement data in the initial linear segment are used to calculate  $\tau_{ave}$  [32]. In our measurements, the diameters of individually tested tubes could not be measured precisely because they are comparable to the resolution limit of the electron beam. Here we calculate the IFSS based on the measured median double-walled tube diameter (i.e.  $D = 2.9$  nm). The average IFSS of the BNNT-silica interface is quantified to be about  $34.7 \pm 8.2$  MPa ( $n = 12$ ). We also calculate the average IFSS value based on the lower and the upper limits of the diameter of double-walled BNNTs (i.e. 1.9 and 3.9 nm) and the results are summarized in table 1.

**Table 1.** Summary of the measured and calculated interfacial strength properties of BNNT-silica interfaces.

	Bi-linear fitting		Shear-lag model					
	Maximum pull-out force (nN)	Estimated critical tube embedded length (nm)	Average interfacial shear strength (MPa)			Maximum interfacial shear strength (MPa)		
			BNNT diameter (nm)			BNNT diameter (nm)		
			1.9	2.9	3.9	1.9	2.9	3.9
BNNT-Silica interface properties	165 ± 15	560	53.1 ± 12.4	34.7 ± 8.2	25.8 ± 6.1	2812 ± 275	1252 ± 122	712 ± 69

## 2.2. Micromechanics modeling of the interfacial load transfer characteristics of BNNT-ceramic interfaces

The evolution of the shear stress on the stretched BNNT-ceramic interface can be divided into two stages: (I) prior to interface debonding, where the interfacial shear stress starts to increase under the external applied loading until the maximum interfacial shear stress that occurs at the tube entry position reaches a threshold limit; the BNNT-ceramic interface is fully-bonded at this stage. (II) Progression of interface debonding, which occurs when the maximum interfacial shear stress reaches the threshold limit; a crack initiates and starts to propagate along the BNNT-ceramic interface. The crack propagation results in a gradual decrease of the bonded length of the BNNT-ceramic interface until the tube is completely pulled out from the matrix. We note that the pull-out force from our single-tube pull-out measurements that were conducted under force-controlled loading reflects the critical load for transition from stage I to stage II. Here we investigate the interfacial load transfer characteristics in both stages and quantify the maximum IFSS value using a micromechanics model.

The schematic in figure 4(a) illustrates the micromechanics model that is employed to predict the interfacial shear stress distribution profile along the BNNT-ceramic interface in Stage I and to determine the maximum IFSS. The schematic in figure 4(b) illustrates the micromechanics model that is employed to predict the interfacial shear stress distribution evolution during the interface debonding process (Stage II). For simplicity, we assume (1) a homogeneous interface between the embedded tube segment and the surrounding silica matrix, with no binding interaction between the debonded tube segment with the matrix, (2) the absence of residual stress for both the tube and matrix before pull-out [36], and (3) both the tube and the ceramic matrix to deform elastically. Load transferred through the BNNT-silica interface dissipates radially and the shear from the BNNT to the ceramic matrix dissipates radially. Significant interfacial shear stress is confined to a thin matrix layer that binds directly to the BNNT surface [34, 43], as indicated by blue shaded regions in figures 4(a) and (b). With this model setup, the interfacial matrix layer is under pure shear deformation.

*Stage I:* The equilibrium of the embedded tube segment along its longitudinal direction is given as

$$\sigma_z \cdot D + 4 \int_{z_0}^{z_L} \tau_i dz = 0, \quad (1)$$

where  $z$  is the coordinate axis,  $z_0$  is the location of the tube's embedded end and  $z_L$  is the tube entry position;  $\sigma_z = E_f \frac{du(z)}{dz}$  is the normal stress in the tube, and  $u(z)$  is the tube's displacement and  $E_f$  is the tube's Young's modulus;  $\tau_i = \frac{E_m}{2(1 + \nu_m)t} \cdot u(z)$  is the interfacial shear stress, and  $E_m$  and  $\nu_m$  are the Young's modulus and the Poisson's ratio of matrix, respectively, and  $t$  is the thickness of the interfacial matrix layer and also the only fitting parameter in the model. By inserting this relationship into equation (1), the governing

equation for the nanotube's displacement becomes

$$D \cdot E_f \frac{d^2u(z)}{dz^2} + 4 \frac{2E_m}{2(1 + \nu_m) \cdot t} u(z) = 0. \quad (2)$$

The boundary condition used in the model includes  $\sigma_z = 0$  at  $z = z_0$ . The stretching force  $P$  shall equal the interfacial shear force on the binding interface, i.e.  $\pi \cdot D \int_{z_0}^{z_L} \tau_i dz = P$ . Equation (2) is solved with the following parameters:  $E_m = 70$  GPa and  $\nu_m = 0.17$  for silica [44];  $E_f = 1.09$  TPa for BNNTs [13].

The blue segment of the curve in figure 4(c) shows the displacement of the tube entry position (i.e. the nanotube length extension) as a function of the applied load for a BNNT-silica interface with  $L = 750$  nm and  $P_{out} = 165$  nN (the measured average plateau force in figure 3). The segment end, which is marked as point #1, corresponds to the onset of interfacial failure (i.e. the applied load reaches the pull-out value). The corresponding IFSS distribution profile is displayed as a blue curve in figure 4(d). The theoretical calculations are based on  $D = 2.9$  nm (the median tube diameter) and  $t = 8.1$  nm (a fitting value). The blue curve in figure 4(d) shows a maximum shear stress ( $\tau_{max}$ ) of about 1.25 GPa. Considering the variation in the measured force plateau, the maximum shear stress of BNNT-silica interface is calculated to be  $1.25 \pm 0.12$  GPa. The remarkably high interfacial shear strength indicates a strong binding interaction on the BNNT-silica interface, which is consistent with prior reports [29, 30, 45]. From the electronic structure point of view, B–N bonds are mostly covalent, but also are highly polarized due to unsymmetrical charge distribution. The electrostatic or Coulomb interactions tend to lead a higher binding interaction. It is noted that the maximum IFSS of BNNT-silica interfaces obtained in this study is much higher than the reported values for BNNT-PMMA and BNNT-epoxy interfaces (i.e. 219 and 323 MPa), indicating a much stronger interfacial binding interactions of BNNTs with silica versus with those two polymers. DFT calculations, which are discussed in detail in section 2.4, confirm that strong binding interactions are formed between BN and silica lattices.

Figure 4(d) also shows that the effective shear stress transfer occurs on a relatively shorter length compared to the entire tube embedded length, which is attributed to the fact that the matrix material (silica) possesses a high Young's modulus. The result also implies that the effective contacts between a BNNT with surrounding ceramic grains likely occur on a smaller area than the value calculated based on the entire embedded length. The maximum shear displacement of the interface matrix layer occurs at the tube entry position,  $u_m$  and is given as  $u_m = u(L) = 2t \cdot \tau_{max} / (E_m / (1 + \nu_m))$ .  $u_m$  is calculated to be about 0.34 nm, which is close to double the Si–O bond length (0.16 nm) [46].

*Stage II:* the aforementioned equilibrium equations in Stage I can be readily extended to Stage II by taking into account the following two factors: (i) the length of the bonded interface decreases as a result of interface debonding. (ii) The interface debonding occurs under the maximum IFSS at the interface debonding front. The maximum displacement of the tube at the

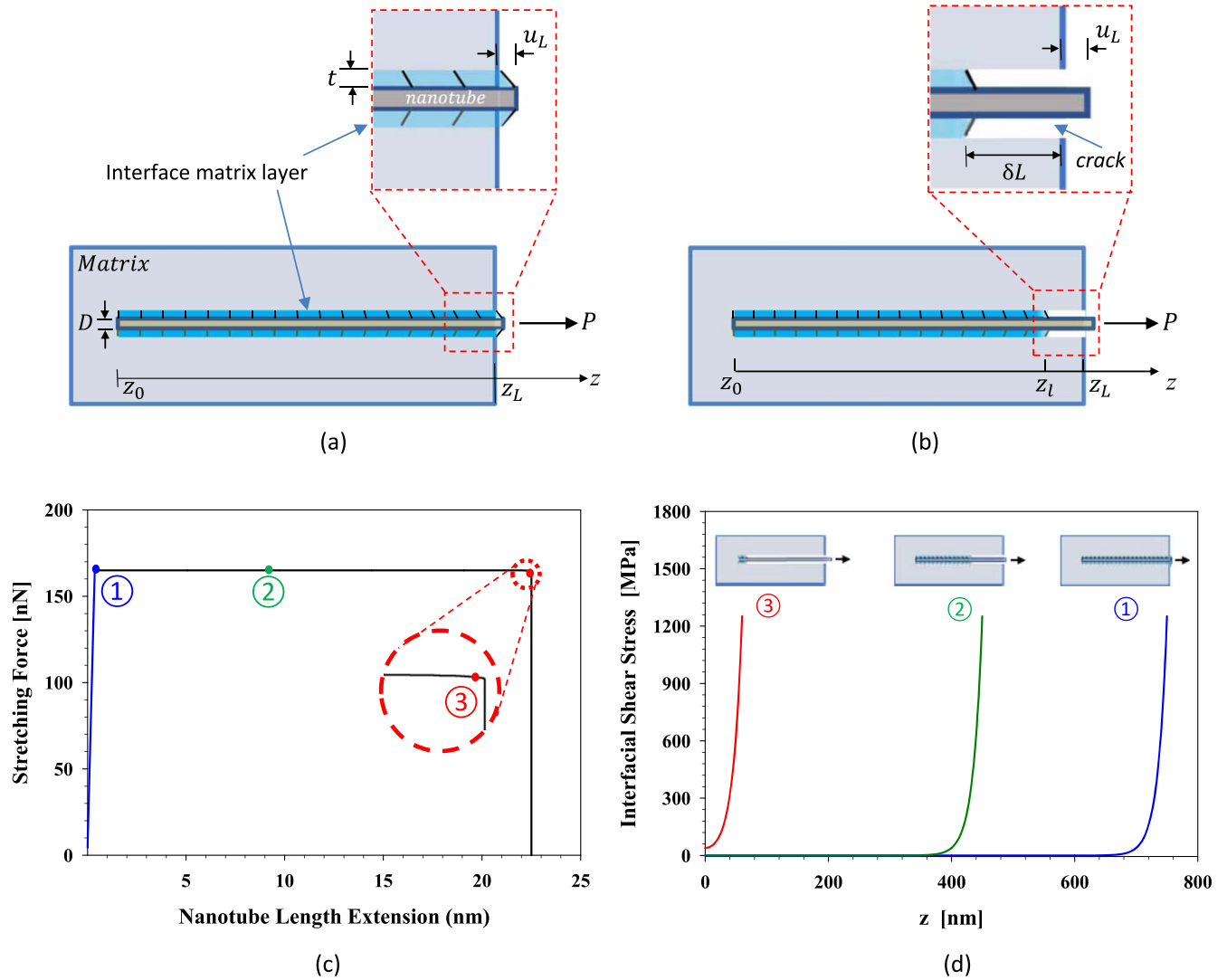


**Figure 4.** The diagrams of shear load transfer on a fully bonded BNNT-silica interface (a) and on a partially debonded BNNT-silica interface (b). The shear deformation in the interfacial ceramic layer (shaded region) is illustrated by the orientation of the added short lines. (c) Theoretical prediction of the nanotube length extension under the stretching force during the whole nanotube pull-out process. (d) Three selected shear stress distribution profiles that correspond to the three marked positions in (c). The insert diagrams in (d) illustrate the corresponding interface debonding front positions. An embedded tube length of 750 nm is assumed in the calculation.

interface debonding front remains unchanged during the whole interface debonding process and equals  $u_m$ .

Once the maximum IFSS at the tube entry position reaches its physical limit, a crack initiates and then propagates towards the embedded tube end, which leads to a reduction of the bonded interface length by  $\delta l$  and an increase of the protruding tube length. The stretching force applied to a partially debonded interface is given by [32],

$$P = \int_{z_0}^{z_i} \tau_i \pi \cdot D dz, \tag{3}$$

where  $z_i = L - \delta l$  is the length of the remaining bonded interface. The corresponding displacement of the tube at its original entry position (i.e.  $z = L$ ) or the tube length extension is given as

$$u(L) = \frac{P \cdot \delta l}{E_f A_f} + u_m, \tag{4}$$

where the first term on the right side of the equation accounts for the elongation of the debonded tube segment and  $A_f$  is the cross-section area of the tube. The length extension of the tube reaches maximum when  $\frac{du(L)}{dP} = 0$ .

The black segment of the curve in figure 4(c) shows the dependence of the pulling force  $P$  on the tube length extension  $u(L)$  during the interface debonding process. It can be seen that the applied force  $P$  is held quite steadily for a substantial increase of  $u(L)$ , which is attributed to the elongation of the increasing debonded tube segment as a result of continuous interface crack propagation. A noticeable drop of  $P$  occurs when the crack front approaches to the embedded tube end and a sharp decrease of  $P$  to zero occurs, which corresponds to the complete pull-out of the entire tube from the matrix. The green and the red curves displayed in figure 4(d) are two selected interfacial shear stress distribution profiles, which correspond to points '2' and '3' marked in

figure 4(c) respectively. The interfacial shear stress distribution displayed by the green curve, which is calculated based on a bonded interface length of 450 nm, is found to follow exactly the same profile as the blue curve. However, the red curve, which is calculated based on a bonded interface length of 60 nm, shows a distinct profile as compared with the blue and green curves. In particular, the interfacial shear stress at the embedded tube end is found to be about 39.5 MPa, as compared with a zero stress shown in the blue and the green curves. The result indicates that the interfacial shear stress transfer is constrained by the reduced interface length, which results in a lower stretching force  $P$ . The area under the stretching force-tube length extension curve represents the amount of dissipated energy during the entire tube pull-out cycle. The findings here are helpful to better understand the evolution of the interfacial shear stress distribution profiles on both fully bonded and partially debonded nanotube-matrix interfaces and the energy dissipation mechanism during the interface debonding process.

### 2.3. Fracture toughness enhancement in BNNT-reinforced Silica CMNC

In this section, we estimate the fracture toughness enhancement of the composite that is ascribed to the energy dissipation during the nanotube pull-out process. Here we assume an ideal tube-reinforced nanocomposite scenario where the nanotubes are perfectly aligned, parallel to one another, and distributed evenly inside the matrix and the orientations of the tube fibers are perpendicular to the crack propagation path, as illustrated in figure 5(a). The fracture toughness enhancement  $\Delta K$  is given by [47, 48],

$$\Delta K = \int_0^\infty \frac{\sqrt{2}P}{\sqrt{\pi r}(A_f + A_m)} dr, \quad (5)$$

where  $A_m$  is the cross-section area of the matrix;  $r$  is the distance of the crack front to a tube and its relationship with the tube elongation is given as [47],

$$u(L) = \frac{2(1 - \nu_m^2)K_{IC}}{E_m} \sqrt{\frac{2r}{\pi}}, \quad (6)$$

where  $K_{IC}$  is the critical stress intensity factor of matrix.

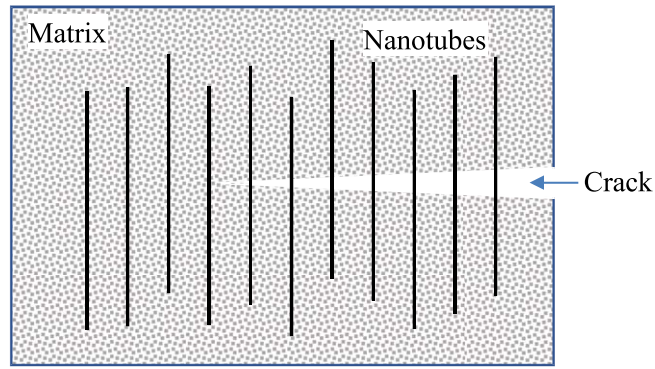
The silica matrix possesses a  $K_{IC}$  value of 0.58 MPa m<sup>1/2</sup> and a density of 2.3 g cm<sup>-3</sup>. We calculate the fracture toughness improvement by considering two types of BNNTs: (1) multi-walled BNNTs of about 40 nm in outer diameter that were employed in [29]; (2) double-walled BNNTs of about 2.9 nm in outer diameter that were employed in the pull-out measurement of the present study. Figure 5(b) shows the calculated fracture toughness improvements by considering BNNTs used in [29] with a tube length of 1 μm and a density of 1.4 g cm<sup>-3</sup> and the measured BNNT-silica interface stress data in the present study, which are contrasted with the reported experimental values. The results show that the discrepancy between the theoretically predicted and experimental fracture toughness improvement is within 24.9%–57.7%. Specifically, the theoretically predicted (experimental) mean values for 1%, 3% and 5% wt BNNTs are 54.2%

(29.3%), 111.2% (53.4%) and 143.8% (108.6%), respectively. Potentially, this discrepancy can be attributed to: (1) non-idealities related to tube dispersion and alignment as well as the presence of structural defects in tubes in the tested composites; (2) the difference in processing and interface conditions between the composites manufactured in [29] and the present study, which may affect the tube-matrix load transfer characteristics and thus the fracture toughness improvement.

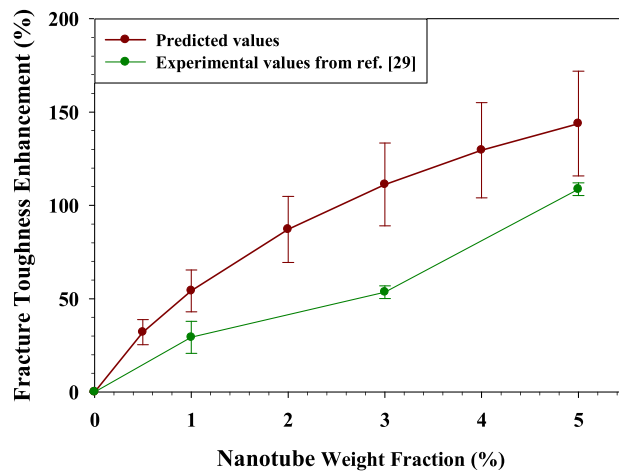
Figures 5(c) and (d) show the calculated fracture toughness improvement by considering the double-walled BNNTs used in the pull-out test with an outer diameter tube of 2.9 nm. The calculation considers a wide range of tube length that are consistent with those of HTP-BNNTs (100 nm–10 μm) and a tube weight concentration of 1%–10%. Figure 5(c) shows the dependences of the fracture toughness enhancement on the nanotube length for a variety of tube weight concentrations. The data show that both the nanotube length and the tube concentration have a substantial impact on the fracture toughness enhancement. Specifically, the predicted fracture toughness enhancement increases linearly with the tube length, indicating the preference of long tubes in order to achieve better durability. Fracture toughness is also more enhanced at larger tube concentrations, however, the dependence trend as displayed in figure 5(d) is not linear. The normalized fracture toughness per unit nanotube weight decreases with an increase of tube concentration. Considering a tube length of one micron, 1%, 3% and 5% tube weight concentrations result in fracture toughness increases of about 67.8%, 134.5%, and 170.7%, respectively, all of which are noticeably higher than the respective values predicted by using the large-diameter BNNTs in [29]. The results clearly show that the usage of BNNTs of smaller diameter will lead to a better fracture toughness improvement performance, which can be qualitatively explained by the fact that in tube-reinforced composites, only the outermost shell of a tube makes contacts with the surrounding matrix and contributes to the load transfer and thus the improvement of the bulk mechanical properties. The results displayed in figures 5(c) and (d) show that a combination of long tubes and high tube concentration will result in substantial fracture toughness improvements. For example, considering a tube length of 5 μm, a 5 wt% BNNT will result in an 867% increase of the fracture toughness. The remarkable value of the predicted property enhancement clearly shows the potentials of BNNTs as reinforcing filler materials for making light, strong and durable ceramic nanocomposites.

### 2.4. DFT calculations of the BNNT-silica binding interaction

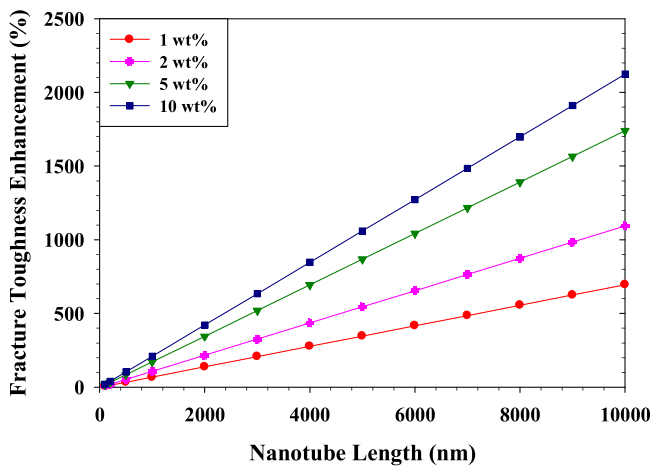
We perform DFT calculations to elucidate the bonding characteristics between SiO<sub>2</sub> and BNNT. The projector augmented wave based pseudopotentials [49, 50] are used to represent the interaction between ionic cores and valence electrons, while the Ceperley–Alder form of the local density approximation (LDA) as parameterized by Perdew–Zunger is adopted for exchange and correlation. For simplicity, we neglect curvature effects [51] and treat BNNTs as equivalent



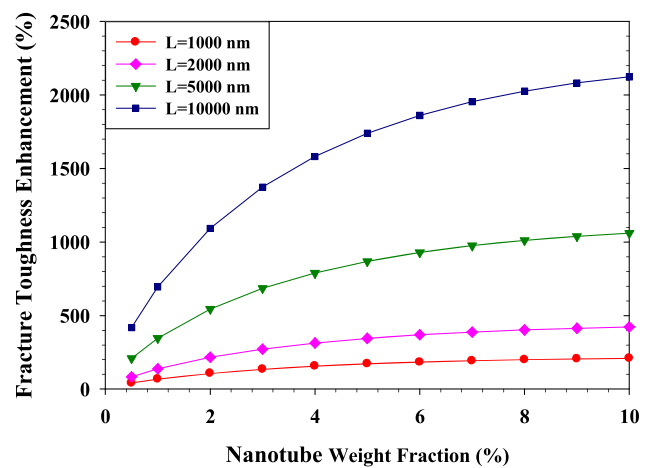
(a)



(b)



(c)



(d)

**Figure 5.** Theoretical prediction of the fracture toughness enhancement in BNNT-reinforced CMNC. (a) Schematic illustration of the fracture zone with bridging BNNTs. (b) Theoretically predicted fracture toughness improvement based on BNNTs employed in [29] and the comparison with the reported experimental values. (c), (d) Theoretically predicted fracture toughness improvement based on HTP-BNNTs that were employed in the present pull-out test: (c) the dependence of fracture toughness enhancement on nanotube length. (d) The dependence of fracture toughness enhancement on nanotube weight fraction.

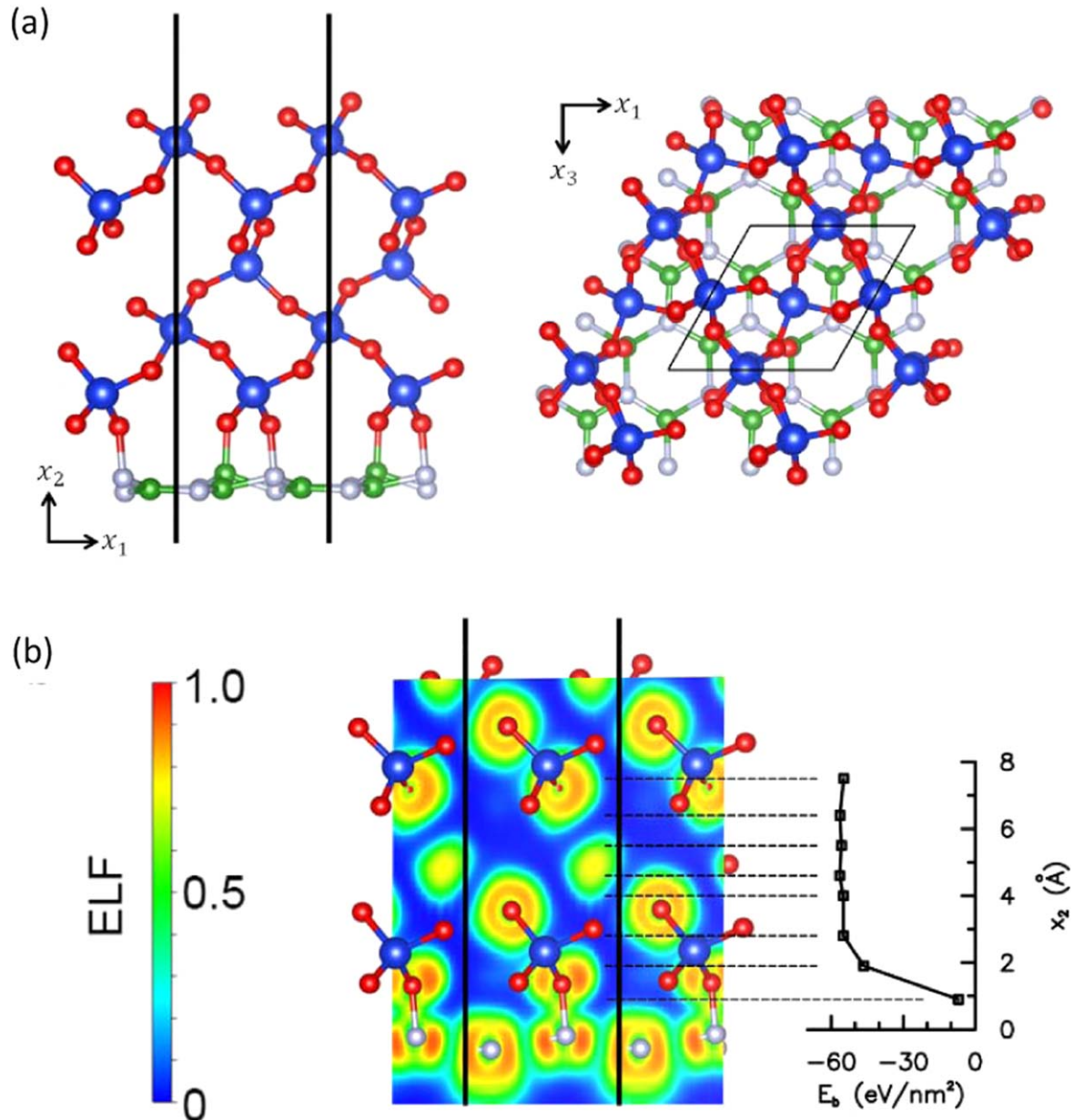


**Figure 6.** First principle calculations of the bonding characteristics along a SiO<sub>2</sub>-hBN (0001) interface. (a) Side and top view of the atomic configuration, with the periodic triclinic supercell in DFT outlined in black. (b) Contours of the electron localized function and distributions of the interfacial energy along the cross-sectional cuts indicated by dashed lines. Blue, red, green, and gray atoms represent Si, O, B, and N, respectively.

2D planar hexagonal boron-nitride (hBN) sheets. Our trigonal supercell comprises of a  $1 \times 1$  unit-cell  $\alpha$  quartz crystal with the normal to the closed-packed (0001) plane aligned with the vertical ( $x_2$ ) axis (see figure 6(a)). Below the O-terminated closed-packed surface of SiO<sub>2</sub>, we include  $2 \times 2$  unit-cells of BN separated by an initial distance of 4 Å. To prevent the BN sheet from also interacting with the periodic image of the top surface of the SiO<sub>2</sub> substrate, a vacuum layer of 12 Å is introduced at the top of the supercell. Throughout our simulations, we adopt an electronic kinetic energy cut-off of 450 eV for the plane wave basis sets describing valence electrons, and we set the energy tolerance criteria for convergence through the conjugate gradient method to 0.1 meV. A gamma centered Monkhorst–

Pack k-point sampling of  $5 \times 1 \times 5$  is used to sample the entire Brillouin zone. After ionic relaxation of the supercell, we obtain lattice constants of 2.47 Å and 4.93 Å for BN and SiO<sub>2</sub>, respectively, versus the equilibrium lattice constants of 2.51 Å and 4.92 Å. The enforced periodicity therefore induces in-plane lattice mismatch strains of 0.18% within the BN sheet and 0.24% within the SiO<sub>2</sub> substrate. Interestingly, the spacing between BN and SiO<sub>2</sub> decreases to 1.48 Å after the equilibration process. The nearest B and N atoms directly below the O-terminated atoms in SiO<sub>2</sub> are also visibly displaced in the out-of-plane direction by 0.425 Å and 0.3 Å, respectively, toward the O atoms.

To gain insights into the chemical bonding characteristics, we examine contours of the electron localized function

(ELF) in figure 6(b), which are observed along a  $x_1$ - $x_2$  cross-sectional cut. Generally, the ELF is a dimensionless, empirical function that generates relatively large values of between 0.5 and 1.0 in regions where electrons are of a high chance of localization, as found in ionic and covalent bonding, while displaying smaller values (less than 0.5) when electrons are delocalized, as in metallic bonding. We observe distinct electron localization (ELF  $\sim 0.75$ ) between the O-terminated atoms of SiO<sub>2</sub> and the B and N atoms of hBN directly below, which confirms the formation of strong B-O and N-O bonds across the interface. We calculate the interfacial energies  $E_b$  along several (0001) planes as marked by dashed lines in figure 6(b), by rigidly separating the surfaces at the designated cross-sections by a distance of 10 Å, and subtracting the per-unit-area energy of the separated system from that of the combined system. Our results for  $E_b$  as a function of distance from the hBN-SiO<sub>2</sub> interface (located at  $x_2 = 0.9$  Å) is shown in figure 6(b) (right). We note that the cohesive energy ( $-E_b$ ) increases almost immediately from 6.98 eV nm<sup>-2</sup> along the hBN-SiO<sub>2</sub> interface to its bulk value of  $\sim 55$  eV nm<sup>-2</sup>. This order-of-magnitude difference in cohesive energy suggests a cleanly separated interface during the pull-out of BNNT, as shown by our TEM imaging in figure 1(g). We remark that the interfacial energy of  $E_b = -6.98$  eV nm<sup>-2</sup> along the hBN-SiO<sub>2</sub> interface is similar to the strong adhesion of  $-6.21$  eV nm<sup>-2</sup> reported by LDA-DFT calculations for graphene and O-terminated SiO<sub>2</sub>. Similar to the strong N-O and B-O bonding across hBN-SiO<sub>2</sub>, the high cohesive energy for graphene-SiO<sub>2</sub> is associated with the formation of strong C-O and C-Si bonds along the interface [52].

### 3. Conclusion

We investigate the nanomechanical strength of BNNT-silica interfaces by using a combined experimental and computational approach. The nanomechanical measurements reveal a remarkable interfacial shear strength of about 1.25 GPa on BNNT-silica interfaces. DFT calculations show strong binding interaction between BN and silica lattices. The fracture toughness of BNNT-silica CMNC is predicted based on the measured interfacial strength property and substantial fracture toughness improvements are demonstrated even at small fraction of filler concentrations. The results demonstrate that BNNTs are excellent reinforcing filler materials for light, strong and durable CMNC that may find usage in many demanding applications, such as those that are involved with harsh thermal, chemical, and/or radiation environments.

### 4. Materials and methods

The BNNTs employed were purchased from BNNT, LLC., and synthesized using HTP methods [37, 38]. The as-received BNNT were separated in deionized water using ultrasonication with the aid of ionic surfactants [15]. The sandwiched silica/BNNT/silica composites were prepared using approaches as

reported in our recent studies [34, 36]. Silica films of 100 nm in thickness in each layer were deposited using an ATC Orion 8-E evaporator system (AJA International Inc.) with a silica target of 99.999% in purity (Kamis Inc.). AFM characterizations were conducted inside an NTEGRA AFM (NT-MDT). SEM and TEM characterizations were conducted using a Supra 55 SEM (Zeiss) and a JEM 2100F TEM (JEOL Ltd), respectively. The *in situ* nanomechanical single-nanotube pull-out experiment were conducted by using a 3D piezo-stage based nanomanipulation technique [53–55] and the detailed experimental setup and operations are reported in [34, 36]. Silicon AFM probes (CSG 01, NT-MDT), acting as the force sensors in the measurements, have a nominal tip radius of 10 nm and individually calibrated spring constants of 0.04–0.09 N m<sup>-1</sup>. The pull-out measurements were conducted with a force resolution of about 0.5–1.0 nN load and a spatial resolution of a few nm. The DFT calculations are conducted using the Vienna *ab initio* Simulation Package.

### Acknowledgments

This work was supported by the United States Air Force Office of Scientific Research—Low Density Materials program under Grant No. FA9550-15-1-0491 and by the National Science Foundation under Grant Nos. CMMI-1537333 (CK) and CMMI-1538162 (HBC). CMD acknowledges fellowship support from the New York NASA Space Grant Consortium. The material characterization and nanomechanical measurements were performed using the facilities in the Analytical and Diagnostics Laboratory at Binghamton University's Small Scale Systems Integration and Packaging Center (S3IP). The DFT calculations were performed using the computational resources provided by TACC (Award No. TG-MSS130007) and the Blue Waters sustained-petascale computing project which is supported by the National Science Foundation (Award Nos. OCI-0725070 and ACI-1238993) and the state of Illinois, USA.

### ORCID iDs

Changhong Ke  <https://orcid.org/0000-0002-5170-9859>

### References

- [1] Cho J, Boccaccini A R and Shaffer M S P 2009 Ceramic matrix composites containing carbon nanotubes *J. Mater. Sci.* **44** 1934–51
- [2] Munro R G 1997 Evaluated material properties for a sintered alpha-alumina *J. Am. Ceram. Soc.* **80** 1919–28
- [3] Rubio A, Corkill J L and Cohen M L 1994 Theory of graphitic boron-nitride nanotubes *Phys. Rev. B* **49** 5081–4
- [4] Chopra N G, Luyken R J, Cherrey K, Crespi V H, Cohen M L, Louie S G and Zettl A 1995 Boron-nitride nanotubes *Science* **269** 966–7

- [5] Treacy M M J, Ebbesen T W and Gibson J M 1996 Exceptionally high Young's modulus observed for individual carbon nanotubes *Nature* **381** 678–80
- [6] Chopra N G and Zettl A 1998 Measurement of the elastic modulus of a multi-wall boron nitride nanotube *Solid State Commun.* **105** 297–300
- [7] Arenal R, Wang M-S, Xu Z, Loiseau A and Golberg D 2011 Young modulus, mechanical and electrical properties of isolated individual and bundled single-walled boron nitride nanotubes *Nanotechnology* **22** 265704
- [8] Hernandez E, Goze C, Bernier P and Rubio A 1998 Elastic properties of C and  $B_xC_yN_z$  composite nanotubes *Phys. Rev. Lett.* **80** 4502–5
- [9] Ghassemi H M, Lee C H, Yap Y K and Yassar R S 2010 Real-time fracture detection of individual boron nitride nanotubes in severe cyclic deformation processes *J. Appl. Phys.* **108** 024314
- [10] Tang D-M, Ren C-L, Wei X, Wang M-S, Liu C, Bando Y and Golberg D 2011 Mechanical properties of bamboo-like boron nitride nanotubes by *in situ* TEM and MD simulations: strengthening effect of interlocked joint interfaces *ACS Nano* **5** 7362–8
- [11] Suryavanshi A P, Yu M-F, Wen J, Tang C and Bando Y 2004 Elastic modulus and resonance behavior of boron nitride nanotubes *Appl. Phys. Lett.* **84** 2527–9
- [12] Golberg D, Costa P M F J, Lourie O, Mitome M, Bai X, Kurashima K, Zhi C, Tang C and Bando Y 2007 Direct force measurements and kinking under elastic deformation of individual multiwalled boron nitride nanotubes *Nano Lett.* **7** 2146–51
- [13] Zhao Y, Chen X, Park C, Fay C C, Stupkiewicz S and Ke C 2014 Mechanical deformations of boron nitride nanotubes in crossed junctions *J. Appl. Phys.* **115** 164305
- [14] Zheng M, Chen X, Park C, Fay C C, Pugno N M and Ke C 2013 Nanomechanical cutting of boron nitride nanotubes by atomic force microscopy *Nanotechnology* **24** 505719
- [15] Zheng M, Chen X, Bae I-T, Ke C, Park C, Smith M W and Jordan K 2012 Radial mechanical properties of single-walled boron nitride nanotubes *Small* **8** 116–21
- [16] Zheng M, Zou L, Wang H, Park C and Ke C 2012 Quantifying the transverse deformability of double-walled carbon and boron nitride nanotubes using an ultrathin nanomembrane covering scheme *J. Appl. Phys.* **112** 104318
- [17] Zheng M, Zou L-F, Wang H, Park C and Ke C 2012 Engineering radial deformations in single-walled carbon and boron nitride nanotubes using ultrathin nanomembranes *ACS Nano* **6** 1814–22
- [18] Kang J H, Sauti G, Park C, Yamakov V I, Wise K E, Lowther S E, Fay C C, Thibeault S A and Bryant R G 2015 Multifunctional electroactive nanocomposites based on piezoelectric boron nitride nanotubes *ACS Nano* **9** 11942–50
- [19] Yamakov V, Park C, Kang J H, Chen X, Ke C and Fay C 2017 Piezoelectric and elastic properties of multiwall boron-nitride nanotubes and their fibers: a molecular dynamics study *Comput. Mater. Sci.* **135** 29–42
- [20] Xiao Y, Yan X H, Cao J X, Ding J W, Mao Y L and Xiang J 2004 Specific heat and quantized thermal conductance of single-walled boron nitride nanotubes *Phys. Rev. B* **69** 205415
- [21] Chen Y, Zou J, Campbell S J and Caer G L 2004 Boron nitride nanotubes: pronounced resistance to oxidation *Appl. Phys. Lett.* **84** 2430–2
- [22] Golberg D, Bando Y, Huang Y, Terao T, Mitome M, Tang C C and Zhi C Y 2010 Boron nitride nanotubes and nanosheets *ACS Nano* **4** 2979–93
- [23] Chen X, Dmichowski C M, Park C, Fay C C and Ke C 2017 Quantitative characterization of structural and mechanical properties of boron nitride nanotubes in high temperature environments *Sci. Rep.* **7** 11388
- [24] Xu Z, Golberg D and Bando Y 2009 Electrical field-assisted thermal decomposition of boron nitride nanotube: experiments and first principle calculations *Chem. Phys. Lett.* **480** 110–2
- [25] Blase X, Rubio A, Louie S G and Cohen M L 1994 Stability and band gap constancy of boron nitride nanotubes *Europhys. Lett.* **28** 335
- [26] Choi S R, Bansal N P and Garg A 2007 Mechanical and microstructural characterization of boron nitride nanotubes-reinforced SOFC seal glass composite *Mater. Sci. Eng. A* **460–461** 509–15
- [27] Xu J-J, Bai Y-J, Wang W-L, Wang S-R, Han F-D, Qi Y-X and Bi J-Q 2012 Toughening and reinforcing zirconia ceramics by introducing boron nitride nanotubes *Mater. Sci. Eng. A* **546** 301–6
- [28] Wang W-L, Bi J-Q, Wang S-R, Sun K-N, Du M, Long N-N and Bai Y-J 2011 Microstructure and mechanical properties of alumina ceramics reinforced by boron nitride nanotubes *J. Eur. Ceram. Soc.* **31** 2277–84
- [29] Du M, Bi J-Q, Wang W-L, Sun X-L and Long N-N 2011 Microstructure and properties of  $SiO_2$  matrix reinforced by BN nanotubes and nanoparticles *J. Alloys Compd.* **509** 9996–10002
- [30] Tatarko P, Grasso S, Porwal H, Chlup Z, Saggar R, Dlouhý I and Reece M J 2014 Boron nitride nanotubes as a reinforcement for brittle matrices *J. Eur. Ceram. Soc.* **34** 3339–49
- [31] Lahiri D, Singh V, Benaduce A P, Seal S, Kos L and Agarwal A 2011 Boron nitride nanotube reinforced hydroxyapatite composite: mechanical and tribological performance and in-vitro biocompatibility to osteoblasts *J. Mech. Behav. Biomed. Mater.* **4** 44–56
- [32] Chen X, Zheng M, Park C and Ke C 2013 Direct measurements of the mechanical strength of carbon nanotube–poly(methyl methacrylate) interfaces *Small* **9** 3345–51
- [33] Chen X, Zhang L, Zheng M, Park C, Wang X and Ke C 2015 Quantitative nanomechanical characterization of the van der Waals interfaces between carbon nanotubes and epoxy *Carbon* **82** 214–28
- [34] Yi C, Chen X, Gou F, Dmichowski C M, Sharma A, Park C and Ke C 2017 Direct measurements of the mechanical strength of carbon nanotube-aluminum interfaces *Carbon* **125** 93–102
- [35] Chen X, Zhang L, Park C, Fay C C, Wang X and Ke C 2015 Mechanical strength of boron nitride nanotube-polymer interfaces *Appl. Phys. Lett.* **107** 253105
- [36] Yi C, Bagchi S, Dmichowski C M, Gou F, Chen X, Park C, Chew H B and Ke C 2018 Direct nanomechanical characterization of carbon nanotubes-titanium interfaces *Carbon* **132** 548–55
- [37] Smith M W, Jordan K C, Park C, Kim J-W, Lillehei P T, Crooks R and Harrison J S 2009 Very long single- and few-walled boron nitride nanotubes via the pressurized vapor/condenser method *Nanotechnology* **20** 505604
- [38] Tian A L et al 2014 Boron nitride nanotube: synthesis and applications *Proc. SPIE* **9060** 1–19
- [39] Chew H B, Moon M-W, Lee K R and Kim K-S 2011 Compressive dynamic scission of carbon nanotubes under sonication: fracture by atomic ejection *Proc. R. Soc. A* **467** 1270–89
- [40] Ke C H, Pugno N, Peng B and Espinosa H D 2005 Experiments and modeling of carbon nanotube-based NEMS devices *J. Mech. Phys. Solids* **53** 1314–33
- [41] Lau K 2003 Interfacial bonding characteristics of nanotube/polymer composites *Chem. Phys. Lett.* **370** 399–405
- [42] Jiang K R and Penn L S 1992 Improved analysis and experimental evaluation of the single filament pull-out test *Compos. Sci. Technol.* **45** 89–103

- [43] Mahesh S, Hanan J C, Üstündag E and Beyerlein I J 2004 Shear-lag model for a single fiber metal matrix composite with an elasto-plastic matrix and a slipping interface *Int. J. Solids Struct.* **41** 4197–218
- [44] Carlotti G, Doucet L and Dupeux M 1997 Elastic properties of silicon dioxide films deposited by chemical vapour deposition from tetraethylorthosilicate *Thin Solid Films* **296** 102–5
- [45] Li D, Zhang C-R, Li B, Cao F and Wang S-Q 2012 Preparation and mechanical properties of unidirectional boron nitride fibre reinforced silica matrix composites *Mater. Des.* **34** 401–5
- [46] Wells A F 2012 *Structural Inorganic Chemistry* (Oxford: Oxford University Press)
- [47] Chen Y L, Liu B, Huang Y and Hwang K C 2011 Fracture toughness of carbon nanotube-reinforced metal- and ceramic-matrix composites *J. Nanomater.* **2011** 1–17
- [48] Tada H, Paris P C and Irwin G R 2000 *The Stress Analysis of Cracks Handbook* 3rd edn (New York: ASME)
- [49] Kresse G and Furthmüller J 1996 Efficiency of *ab initio* total energy calculations for metals and semiconductors using a plane-wave basis set *Comput. Mater. Sci.* **6** 15–50
- [50] Blöchl P E 1994 Projector augmented-wave method *Phys. Rev. B* **50** 17953–79
- [51] Rohmann C, Sun Q and Searles D J 2016 Interaction of Al, Ti, and Cu atoms with boron nitride nanotubes: a computational investigation *J. Phys. Chem. C* **120** 3509–18
- [52] Hossain M Z 2009 Chemistry at the graphene-SiO<sub>2</sub> interface *Appl. Phys. Lett.* **95** 143125
- [53] Ke C H and Espinosa H D 2006 *In situ* electron microscopy electromechanical characterization of a bistable NEMS device *Small* **2** 1484–9
- [54] Ke C, Zheng M, Zhou G, Cui W, Pugno N and Miles R N 2010 Mechanical peeling of free-standing single-walled carbon nanotube bundles *Small* **6** 438–45
- [55] Zheng M and Ke C 2010 Elastic deformation of carbon-nanotube nanorings *Small* **6** 1647–55